Localised failure of geomaterials: how to extract localisation band behaviour from macro test data

LINH A. LE*, GIANG D. NGUYEN†, HA H. BUI‡ and JOSÉ E. ANDRADE§

The formulation and calibration of constitutive models for geomaterials require material behaviour from experiments under a wide range of triaxial loading conditions. However, failure of geomaterials usually involves localisation of deformation that leads to very strong inhomogeneous behaviour. Therefore, the experimentally measured macro (specimen) behaviour is a mix between very different responses inside and outside the localisation zone and thus should not be used as a true representation of the material responses. This paper proposes a theoretical framework that provides links between mechanical responses inside and outside the localisation band, alongside their contributions toward the overall behaviour of a specimen undergoing localised deformation. This meso–macro connection allows the quantification of behaviour inside the localisation band, which is the main source of material inelasticity, from experimentally measured specimen behaviour. Correlation between the thickness of the localisation band and its behaviour is shown, bounded by a unique stress–deformation relationship describing the behaviour of an idealised zero-thickness localisation band.

KEYWORDS: constitutive relations; plasticity; strain; stress path

INTRODUCTION

Strain localisation is a common failure mode of geomaterials under various loading conditions (Lee & Haimson, 2011; Alikarami *et al*., 2015; Lommatzsch *et al*., 2015; Ma & Haimson, 2016; Vachaparampil & Ghassemi, 2017). With the help of advanced techniques like X-ray tomography and digital image correlation (DIC), recent studies (Alshibli *et al*., 2017; Salvatore *et al*., 2017; Amirrahmat *et al*., 2018, 2019; Druckrey *et al*., 2018) have shown that the deformation inside the localisation zone dominates the macro volumetric and shear deformation of specimens. Localisation of deformation in an initially homogeneous specimen leads to the formation of two zones with finite sizes and distinct responses (i.e. localisation band and surrounding bulk material). Owing to this difference, the specimen homogeneity is lost and the specimen's responses are mixtures of material and structural properties. In such cases, specimen responses involve the size and mechanical behaviour of both the localisation band and the bulk material, as well as the band orientation and boundary conditions. In this sense, stresses and strains calculated from quantities measured at the boundaries of the specimen (or obtained from volume change of the specimen, for the case of volumetric strain) are just volume-averaged quantities and cannot correctly represent the true material behaviour. As a consequence, it is fundamentally incorrect to use these volume-averaged quantities for the calibration or validation of continuum models based on critical state soil mechanics, given this theory is valid only inside the shear band (Desrues *et al*., 2018), where the assumption of homogeneous deformation can still be relatively reasonable.

The importance of localised failure and explicit incorporation of shear band properties (behaviour, orientation and size) in constitutive modelling of geomaterials have been addressed in several studies (Nguyen *et al*., 2012, 2014, 2016a, 2016b, 2017; Haghighat & Pietruszczak, 2015, 2016; Pietruszczak & Haghighat, 2015; Moallemi & Pietruszczak, 2017; Mohammadi & Pietruszczak, 2019; Tran *et al*., 2019; Wang *et al*., 2019; Nguyen & Bui, 2020). These models possess a shear band and corresponding properties, embedded in the constitutive structure, making them able to generate the macro responses from given properties of both the shear band and its surrounding volume. However, the lack of an explicit link to work out the shear band behaviour, which could be reasonably considered as true material behaviour, from conventional multi-axial tests makes the calibration of these models difficult. Although this difficulty can be partly alleviated by the use of fracture energies representing the dissipation capacity of the localisation band (e.g. Nguyen *et al*., 2014; Mir *et al*., 2015; Le *et al*., 2017, 2018, 2019; Mir, 2017; Moallemi & Pietruszczak, 2017; Le, 2019; Tran *et al*., 2019; Wang *et al*., 2019), the use of such scalar properties still impairs the calibration and prediction of these models. This is because, for a given fracture energy value, as the area under the stress–displacement curve, it is possible in principle to have an infinite number of curves representing the shear band (or crack) behaviour. It is also worth mentioning that among the constitutive models listed above, those (Nguyen *et al*., 2016b, 2017) based on breakage mechanics (Einav, 2007a, 2007b) can also overcome the challenges of calibration because all their parameters can be obtained from isotropic compression tests under homogeneous deformation. However, this is only possible in dealing with compaction localisation under high confining pressures where the validity of these models can be well justified.

In the current paper, the authors propose a simple, yet effective and versatile, approach for analysing experimental data to obtain both kinematic (i.e. strain, displacement jump)

Manuscript received 3 April 2020; revised manuscript accepted 12 November 2020.
Discussion on this paper is welcomed by the editor.
* School of Civil, Environmental and Mining Engineering, The University of Adelaide, Adelaide, SA, Australia.
† School of Civil, Environmental and Mining Engineering, The University of Adelaide, Adelaide, SA, Australia (Orcid:0000-0003-2348-7563).
‡ Department of Civil Engineering, Monash University, Clayton, VIC, Australia.
§ Department of Mechanical and Civil Engineering, California Institute of Technology, California, USA.

and static (i.e. stress, traction) behaviour of the localisation band and its surrounding bulk. Based on the constitutive structure, proposed in the so-called double-scale approach (Nguyen *et al.*, 2012, 2014, 2016a; Nguyen & Bui, 2020), the links between behaviour inside the localisation band and the volume-averaged responses of the whole specimen can be explicitly established. The stresses inside and outside the localisation band can thus be obtained from the deformation data and macro stresses measured in experiments. This bridges the gap of knowledge in experimental studies where full-field strains can be obtained with reasonable reliability, but stress fields cannot be. The proposed approach is tailored for analysing triaxial test data on sand and soft rocks, with further kinematic and static assumptions required due to the lack of data from conventional triaxial tests. The parametric study on the correlation between the shear band thickness and its behaviour shows a unique relationship between stresses at the boundary of the shear band and corresponding relative displacement between its two sides. This unique relationship can be used to describe the behaviour of the localisation band under appropriate conditions (e.g. thin shear band).

EXPERIMENTAL OBSERVATIONS AND THE NEED FOR A THEORETICAL FRAMEWORK CONNECTING MESO–MACRO BEHAVIOUR

The keys for analysing experimental data of localised failures can be obtained from examining typical results of a triaxial test, conducted on Hostun sand, associated with X-ray tomography and DIC, as shown in Fig. 1 (Alikarami *et al.*, 2015). The figure shows a rapid increase in shear stress, reaching its peak and gradually coming to a residual state. The volumetric strain is shown to experience a short period of compaction before quickly reducing (dilating) and reaching its stable state. The strain profiles, obtained from DIC (Fig. 1(b)), indicate that the deformations of the specimens are mainly governed by what happens inside the localisation band, while the zone outside the band (bulk) undergoes relatively small deformation. Both incremental shear and volumetric strain fields from experiments indicate that a finite-thickness shear band appears from early stages, even before stress reaches its peak (see also Alshibli *et al.*, 2017; Desrues *et al.*, 2018; Druckrey *et al.*, 2018; Amirrahmat *et al.*, 2019). Experimental results measured by strain gauges attached directly on sandstone specimens (see Lee & Haimson, 2011; Ma & Haimson, 2016) and DIC analyses (Dawidowski *et al.*, 2015; Verma *et al.*, 2019) show that the bulk material undergoes compaction at first and then expansion along an elastic trajectory due to the relaxation of stress in the post-peak stage.

Since there are significant differences in behaviour between the localisation band and the outer bulk material, the stress and strain measured in experiments should not be simply taken as the intrinsic material behaviour. For example, given the deformed shape in Figs 2(a) and 2(b), the stresses measured on the boundaries of the specimen (see Figs 2(c) and 2(d)), are not good representatives of the material behaviour, as they are mixtures of responses inside and outside the localisation band. Similarly, as seen from the deformed shape in Fig. 2(b), the averaged axial strain of the specimen is governed not only by axial deformation, as normally

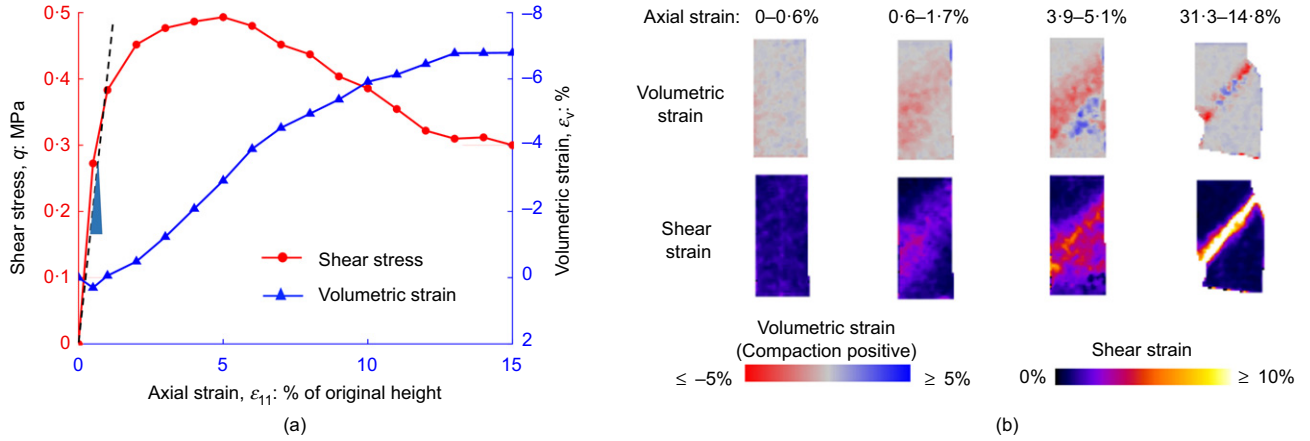

Fig. 1. Behaviour of dry Hostun sand in triaxial tests under confinement of 100 kPa: (a) shear stress and volumetric strain plotted against axial strain; (b) contours of incremental shear and volumetric strains (Alikarami *et al.*, 2015). A full-colour version of this figure can be found on the ICE Virtual Library (www.icevirtuallibrary.com)

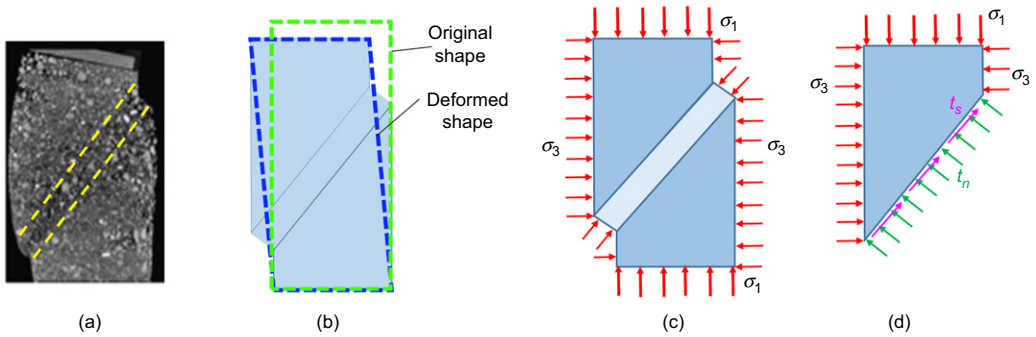

Fig. 2. Illustration of the relationship between measured stress/deformation and shear band behaviour: (a) final failure shape of dry Hostun sand specimen under triaxial loading (Alikarami *et al.*, 2015); (b) idealised deformed shape; (c) stresses at the boundaries; (d) equilibrium

considered, but also by shear deformation induced by an inclined localisation band. Therefore, the behaviour and contributions of these two components should be distinguished by properly interpreting and analysing the measured data. To this end, a meso–macro relationship to connect the responses inside the localisation band with the averaged (macro) responses is needed and will be presented in the next section.

THE PROPOSED MESO–MACRO CONNECTION

In this section, fundamental relationships to connect responses at meso- and macro-scale are presented, together with a specific application to analysing the experimental results of triaxial tests. The readers are referred to the double-scale approach (Nguyen *et al.*, 2012, 2014, 2016a; Nguyen & Bui, 2020) for more details on the formulation and modelling aspects.

Fundamental relationships

The approach is constructed based on a volume element, Ω, featuring a localisation band with inclined angle θ as illustrated in Fig. 3. The band is characterised by its normal vector $\boldsymbol{n}$, surface area A and thickness h, all of which can be determined from experiments with the assumption of a planar localisation band (Fig. 3). The strain increment inside the localisation band ($\delta\boldsymbol{\varepsilon}^{\mathrm{i}}$) can be expressed in terms of the homogeneous strain increment of the bulk material ($\delta\boldsymbol{\varepsilon}^{\mathrm{o}}$) and a kinematically enhanced strain rate component (Neilsen & Schreyer, 1993) as

$$\delta\boldsymbol{\varepsilon}^{\mathrm{i}} = \delta\boldsymbol{\varepsilon}^{\mathrm{o}} + \frac{1}{h}(\boldsymbol{n}\otimes\delta\boldsymbol{u})^{s} = \delta\boldsymbol{\varepsilon}^{\mathrm{o}} + \frac{1}{2h}(\boldsymbol{n}\otimes\delta\boldsymbol{u} + \delta\boldsymbol{u}\otimes\boldsymbol{n}) \quad (1)$$

in which $\delta\boldsymbol{u}$ is the incremental displacement jump vector across the localisation band. It should be noted that the superscripts 'i' and 'o' in these equations simply denote 'inner localisation band' and 'outer bulk material' which are the subjects being referred to. The macro volume-averaged strain increment of the whole specimen ($\delta\boldsymbol{\varepsilon}$) can then be expressed as a linear combination of $\delta\boldsymbol{\varepsilon}^{\mathrm{i}}$ and $\delta\boldsymbol{\varepsilon}^{\mathrm{o}}$, following mixture theory:

$$\delta\boldsymbol{\varepsilon} = f\,\delta\boldsymbol{\varepsilon}^{\mathrm{i}} + (1-f)\delta\boldsymbol{\varepsilon}^{\mathrm{o}} \quad (2)$$

where $f = hA/\Omega$ is the volume fraction of the band calculated from other measurements in experiments (see Fig. 3). Using the virtual work equation (Hill, 1963) in the form, $\boldsymbol{\sigma} : \delta\boldsymbol{\varepsilon} = f\,\boldsymbol{\sigma}^{\mathrm{i}} : \delta\boldsymbol{\varepsilon}^{\mathrm{i}} + (1-f)\boldsymbol{\sigma}^{\mathrm{o}} : \delta\boldsymbol{\varepsilon}^{\mathrm{o}}$, in combination with equations (1) and (2), the following equalities can be obtained (Nguyen *et al.*, 2016a):

$$\boldsymbol{t} = \boldsymbol{t}^{\mathrm{i}} = \boldsymbol{t}^{\mathrm{o}} \quad (3)$$

$$\boldsymbol{\sigma} = f\,\boldsymbol{\sigma}^{\mathrm{i}} + (1-f)\boldsymbol{\sigma}^{\mathrm{o}} \quad (4)$$

where $\boldsymbol{t} = \boldsymbol{\sigma}\cdot\boldsymbol{n}$, $\boldsymbol{t}^{\mathrm{i}} = \boldsymbol{\sigma}^{\mathrm{i}}\cdot\boldsymbol{n}$ and $\boldsymbol{t}^{\mathrm{o}} = \boldsymbol{\sigma}^{\mathrm{o}}\cdot\boldsymbol{n}$ are the tractions associated with, respectively, volume-averaged stress ($\boldsymbol{\sigma}$), stress inside ($\boldsymbol{\sigma}^{\mathrm{i}}$) and outside ($\boldsymbol{\sigma}^{\mathrm{o}}$) the localisation band. With the assumption of homogeneous behaviour inside and outside the localisation band, further connections between responses at meso- and macro-scale can be established from these fundamental relationships, giving rise to the calculation of quantities at one scale given those at the other scale (see Appendix). However, in commonly used experiments such as triaxial tests, the data obtained are not solely measured for macro- or meso-scale, but a mixture of both depending on the way the experiments are executed. The measured data, in these cases, should be carefully interpreted and analysed based on the fundamental relationships above to calculate other unknown quantities. It should also be noticed that since the approach is formulated based on the failure involving a relatively straight localisation band commonly exhibited in experiments, it can be applied to a large volume of existing experimental data. For more complex localised failure patterns (e.g. Desrues *et al.*, 1996), further developments are needed to obtain reasonable results (e.g. initial work on localised failure without a clear band in Pour *et al.* (2020)). This is beyond the scope of the current paper and will be addressed in the authors' future work.

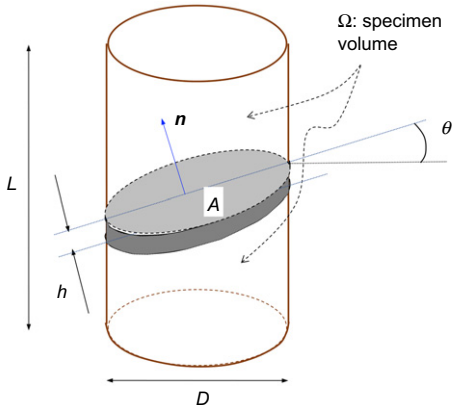

Fig. 3. Localised failure in a cylindrical specimen (after Nguyen *et al*, 2016b)

Application to triaxial tests

In most triaxial tests, the axial stress σ_{11}, alongside pre-defined horizontal stress $\sigma_{22} = \sigma_{33}$, are recorded. Axial strain, ε_{11}, is also usually measured by using linear variable differential transformers (LVDTs). Also, from the volume change of pore fluid in specimens or with the help of three-dimensional (3D) images tomography, the volumetric strain, ε_{v}, can be determined. The task then is to map those quantities into the connection described above and to determine the other quantities.

Determination of strains inside the localisation band. The three measured stresses should be considered as stresses of the bulk ($\boldsymbol{\sigma}^{\mathrm{o}}$), since this zone can be reasonably assumed to undergo relatively small shear deformation compared to the shear band (Figs 2(a) and 2(b)). Because the axial and volumetric strain are measured based on the overall deformation of the whole specimen, they should be considered as volume-averaged deformation. Up to this point, the inputs for the analysis include bulk stress ($\boldsymbol{\sigma}^{\mathrm{o}}$) the volume-averaged axial and volumetric strain (ε_{11}, ε_{v}) and the expected outputs are stresses, strains inside the localisation band, together with volume-averaged stresses and strains.

The first step is to determine the elastic properties of the material based on beginning steps of the loading where the whole specimen can still be assumed to be homogeneous and in the elastic range, as illustrated in Fig. 1(a). By using the triaxial conditions: $\delta\varepsilon_{22} = \delta\varepsilon_{33}$; $\delta\sigma_{22} = 0$ for the general Hooke's law, the bulk modulus K can be computed from the axial stress and strain as

$$K = \frac{[2+(2\alpha/3)]}{[2+(2\alpha/3)][1+(4\alpha/3)] - 2[1-(2\alpha/3)]^2}\frac{\delta\sigma_{11}}{\delta\varepsilon_{11}} \quad (5)$$

where $\alpha = 3(1-2\upsilon)/2(1+\upsilon)$ with υ being the Poisson's ratio. For the case of soil/sand, the bulk modulus K is usually

assumed to be pressure dependent: $K = vp'/\kappa$ (Wood, 1991), where $v = 1/(1-n)$ is the specific volume change, calculated from porosity n. Therefore parameter κ can be obtained as

$$\kappa = \frac{vp'}{K} \tag{6}$$

From these elastic properties, the standard elastic tangent stiffness $\boldsymbol{D}^{\mathrm{o}}$ can be computed. As the behaviour of the bulk material is considered to be elastic, its strain increment can be calculated in a straightforward way from measured stress as

$$\delta\boldsymbol{\varepsilon}^{\mathrm{o}} = \boldsymbol{D}^{\mathrm{o}-1} : \delta\boldsymbol{\sigma}^{\mathrm{o}} \tag{7}$$

Substituting equation (1) into equation (2) for the calculation of volumetric strain increment $\delta\varepsilon_{\mathrm{v}}$ and solving for normal displacement jump increment δu_n in the local coordinate system, one obtains

$$\delta u_n = \left(\delta\varepsilon_{\mathrm{v}} - \delta\varepsilon^{\mathrm{o}}_{11} - \delta\varepsilon^{\mathrm{o}}_{22} - \delta\varepsilon^{\mathrm{o}}_{33}\right)\frac{h}{f} \tag{8}$$

Using equations (1) and (2) for strain increment $\delta\varepsilon_{11}$, the shear displacement jump increment in the local coordinate system (O*nts* in Fig. 4) can be calculated by

$$\delta u_s = \frac{\delta u_n \cos\theta - \left[\delta\varepsilon_{11} - \delta\varepsilon^{\mathrm{o}}_{11}\right]L}{\sin\theta} \tag{9}$$

It is noted that in the above derivation, the transformation of displacement jump increment from the global coordinate system (O123) to the local one (O*nts* in Fig. 4), $\delta u_1 = \delta u_n \cos\theta - \delta u_s \sin\theta$, is used. The incremental displacement jump vector in the global coordinate system, $\delta\boldsymbol{u}$, can then be calculated from those in the local coordinate system. Strain increment inside the localisation band, $\delta\boldsymbol{\varepsilon}^{\mathrm{i}}$ and volume-averaged strain increment, $\delta\boldsymbol{\varepsilon}$ can then be calculated in a straightforward way by equations (1) and (2).

Determination of stresses inside the localisation band. Using the second equality in equation (3), the traction increment on the local coordinate system of the localisation band, $\delta\boldsymbol{t}^{\mathrm{i}}_{\mathrm{local}}$, can be calculated as

$$\delta\boldsymbol{t}^{\mathrm{i}}_{\mathrm{local}} = \mathbf{R}\cdot\delta\boldsymbol{\sigma}^{\mathrm{o}}\cdot\boldsymbol{n} \tag{10}$$

where $\mathbf{R}$ is the standard transformation matrix from the global to the local coordinate system. From the equilibrium shown in the local coordinate system (see Fig. 4), the normal and shear stress increments inside the localisation band can be obtained as

$$\delta\sigma^{\mathrm{i}}_n = \delta t_n \text{ and } \delta\sigma^{\mathrm{i}}_{ns} = \delta t_s \tag{11}$$

It is reasonable to assume that the normal stress in the t-axis is equal to the confining pressure $\sigma^{\mathrm{i}}_t = \sigma_{33}$ ($\delta\sigma^{\mathrm{i}}_t = \delta\sigma_{33} = 0$) and other shear stresses are zero $\sigma^{\mathrm{i}}_{st} = \sigma^{\mathrm{i}}_{nt} = 0$ due to symmetry. As illustrated in Fig. 4, the total form of σ^{i}_s can be calculated from the equilibrium of a segment cut from the side of the specimen. Since it is complicated to calculate σ^{i}_s from the segment in three dimensions, the calculation of this stress is approximated from a simplified equilibrium in two dimensions (see Fig. 4) for simplicity. The authors acknowledge that this is a strong assumption, the consequence of which is yet to be explored, given insufficient data from experiments and the challenges in analysing a boundary value problem analytically. In association with the current deformation of the localisation band (reflected through the angle β), σ^{i}_s is calculated as

$$\sigma^{\mathrm{i}}_s = \sigma^{\mathrm{i}}_{ns}\tan\beta + \sigma_{33} \tag{12}$$

in which $\tan\beta$ is calculated from the deformation as

$$\tan\beta = \frac{h\tan\theta - u_s}{h + u_n} \tag{13}$$

It should be noted that this approximation of σ^{i}_s is only reasonable when h is relatively large compared to u_s. For the case of more brittle materials, namely, sandstone or concrete, h is usually very small (i.e. $h \to 0$), the angle β calculated in this manner would become negative (i.e. $\tan\beta \to -u_s/u_n$) leading to a significant reduction of σ^{i}_s and an increase of shear stress, q. A possible alternative to avoid this unphysical increase of shear stress is to assume that σ^{i}_s remains unchanged once localisation initiates. This alternative will be investigated further by way of an example of sandstone presented in the later section entitled 'Analysing data from tests by Takano *et al.* (2015)'. Now that the stress increments of the localisation band and the bulk material are known, the increment of volume-averaged stress can be calculated using the incremental form of equation (4).

ANALYSIS OF EXPERIMENTAL DATA

Analysing data from tests by Alikarami et al. *(2015)*

In this section, the proposed framework is applied to analysing the results of triaxial tests conducted on cylindrical samples of Ottawa sand with a diameter of 11 mm and a height of 22 mm under three confining pressure levels;

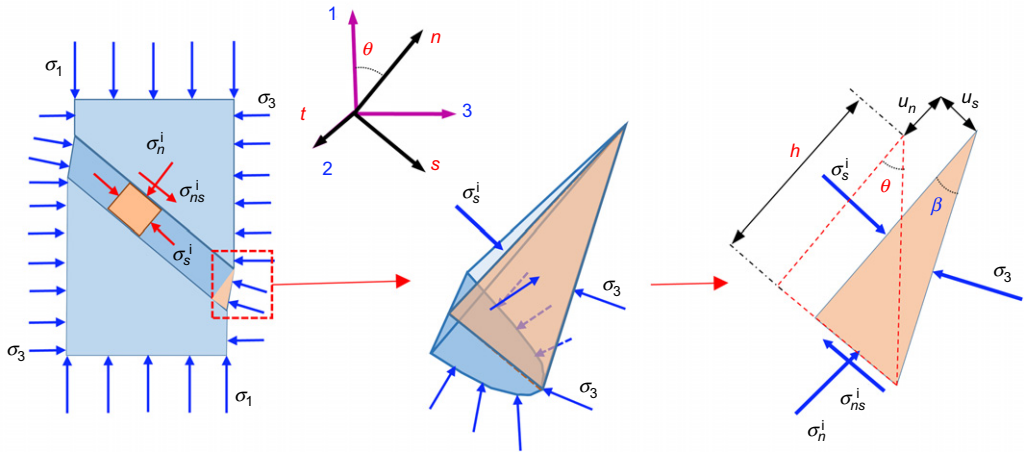

Fig. 4. The balance of local stresses inside and outside the localisation band

$\sigma_{33} = 0{\cdot}1$, 4 and 7 MPa. From the experimental results, the localisation band thickness, failure angle and initial porosity of each test case are shown in Table 1.

With Poisson's ratio $\upsilon = 0{\cdot}2$, the elastic properties of each specimen are calibrated and presented in Table 1. It can be seen that the values of computed parameter κ from separate experimental results are comparable with each other. From the original data set, the results obtained show the difference in deformation across the specimen (see Fig. 5). The onset of localisation can be identified from the bifurcation of deformation, which occurs at $\varepsilon_{11} = 3$–5%, illustrated by the dashed box in Fig. 5. This is close to experimental observations by Alikarami *et al.* (2015) using X-ray tomography and DIC. After the localisation band appears, the axial strain inside the localisation band, ε_{11}^{i}, increases rapidly, while the strain of the bulk material, ε_{11}^{o}, decreases (see the insets in Fig. 5) due to relaxation as analysed in the earlier section entitled 'Experimental observations and the need for a theoretical framework connecting meso–macro behaviour'.

The evolution of volumetric strain, plotted in Fig. 6, shows that the bulk material undergoes compaction at first and then small expansion due to stress relaxation, as expected. The volumetric strain of the localisation band, on the other hand, experiences a large expansion due to dilation. This result from the analysis is supported by experimental observations where porosity inside the localisation band is seen to increase in later stages of loading (Fig. 9 in Alikarami *et al.* (2015)). The combination of these two components (i.e. localisation band and outer bulk material) results in the volume-averaged volumetric strain of the whole specimen (see Fig. 6). The proposed simple scheme can also capture the change of volumetric strain over a period of loading span, indicated as the space between two dashed lines in Fig. 6. In early stages of the tests, the volumetric strain inside the localisation band shows negative increments, corresponding to the dilation. Toward the end of the experiments, the volumetric strain in the band either remains constant under low confinements (its increment is zero as shown in Fig. 6(a)) or becomes compactive under high confinements (its increment is positive as shown in Figs 6(b) and 6(c)). These results from the analysis are consistent with the incremental volumetric strain fields captured by DIC (see Fig. 6). Fig. 7 shows the jumps of both normal stress (σ_s) and normal strain (ε_s) in the local coordinate system for the case $\sigma_{33} = 4$ MPa. These jumps indicate the distinct behaviour of the band compared to that of its surrounding material described above. The plots also show the onset of the localisation, marked by a bifurcation of responses (see Figs 7(a) and 7(b)).

Table 1. Localisation band geometries and obtained elastic properties of the material

	Band thickness, h: mm	Failure angle, θ: degrees	Porosity, n: %	Modulus, K: MPa	Parameter, κ
$\sigma_{33} = 0{\cdot}1$	3·9	52	32·1	10·6	0·014
$\sigma_{33} = 4$	4·8	50	29·1	294	0·019
$\sigma_{33} = 7$	4	49	27·3	599·2	0·017

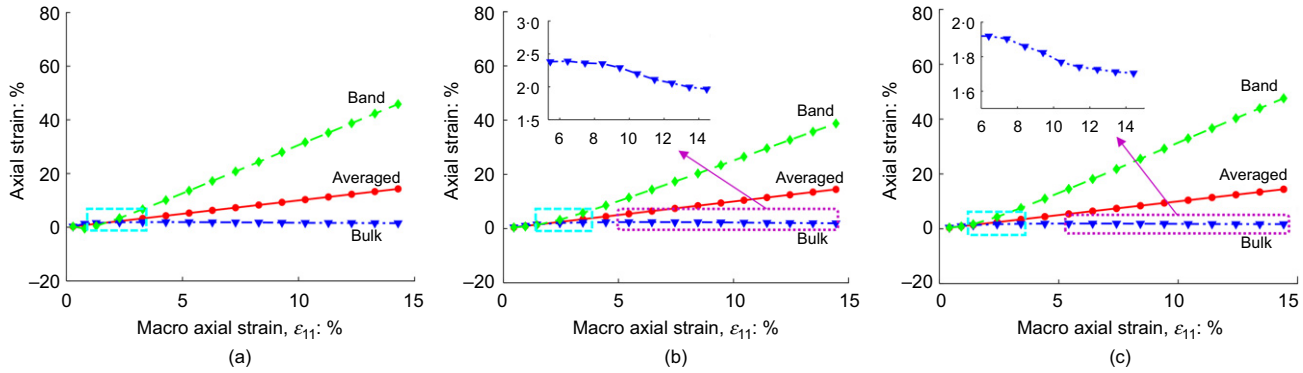

Fig. 5. Vertical (axial) strains inside and outside the localisation band: (a) $\sigma_{33} = 0{\cdot}1$ MPa; (b) $\sigma_{33} = 4$ MPa; (c) $\sigma_{33} = 7$ MPa

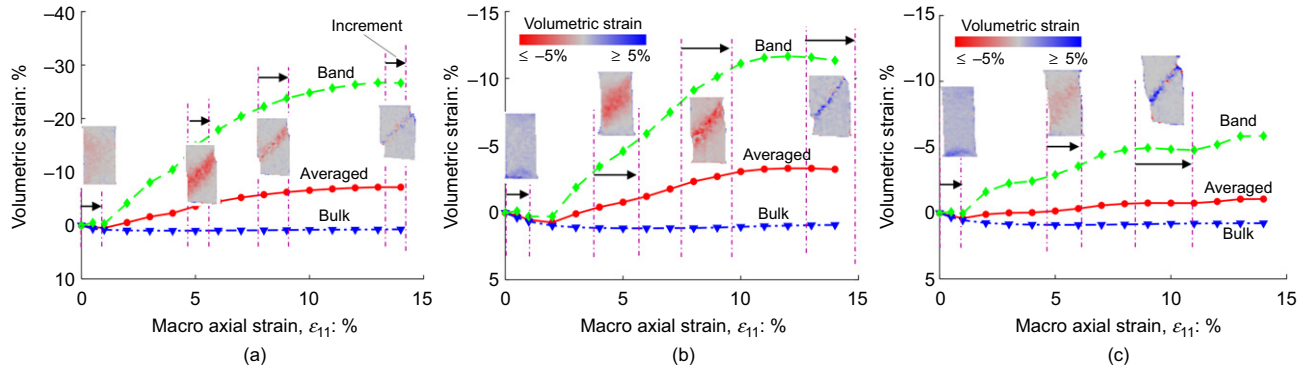

Fig. 6. Volumetric strains inside and outside the localisation band (compaction to be positive): (a) $\sigma_{33} = 0{\cdot}1$ MPa; (b) $\sigma_{33} = 4$ MPa; (c) $\sigma_{33} = 7$ MPa, alongside incremental volumetric strain fields measured by DIC (Alikarami *et al.*, 2015). A full-colour version of this figure can be found on the ICE Virtual Library (www.icevirtuallibrary.com)

The shear stress obtained, $q = \sqrt{3J_2}$ (J_2 being the second invariant of the deviatoric stress tensor) plotted in Fig. 8 shows shear behaviour of different components in the specimens. While the shear stress of the bulk material evolves along the elastic trajectory, the shear stress of the localisation band undergoes softening with much larger deformation. The volume-averaged behaviour is a combination of these two responses. The traction–displacement jump behaviour in the local coordinate system of the localisation band, plotted in Fig. 9, shows that an increase of confining pressure leads to higher normal traction on the failure plane, reducing the dilation under shearing.

The stress paths obtained for the localisation band, plotted in Fig. 10, show a clear deviation from the conventional path, $\Delta q/\Delta p = 3$ ($p = I_1/3$ with I_1 being the first invariant of the stress tensor), which are usually considered as stress paths of the material in triaxial stress condition. The maximum and residual shear stress inside the localisation band can be used to formulate a so-called yield-failure loading function controlling the stress evolution from initial yield to final failure (dashed black line in Fig. 10(a)). Alternatively, the traction path (i.e. t_n–t_s path), as shown in Fig. 10(b), can also be used for formulation and calibration of this yield-failure surface. These stress paths, together with the behaviour obtained (i.e. Figs 8 and 9), provide a rigorous basis for building a good constitutive model for geomaterials, as demonstrated in Le *et al.* (2018).

Analysing data from tests by Takano et al. (2015)

The experimental data used in this section were obtained from cylindrical specimens with a diameter of 50 mm and a

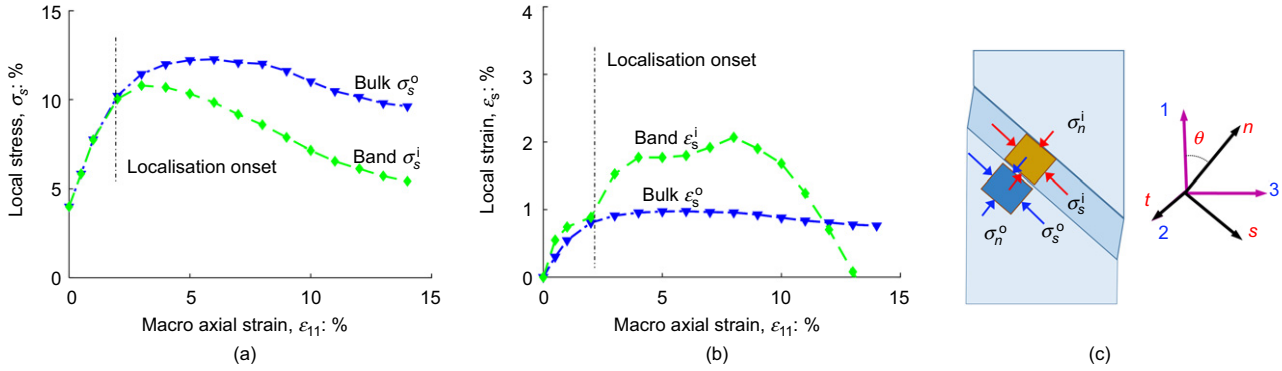

Fig. 7. Responses in the local coordinate system (σ_{33}= 4 MPa): (a) normal stress parallel to the band σ_s; (b) normal strain parallel to the band ε_s; (c) local stress inside and outside the localisation band

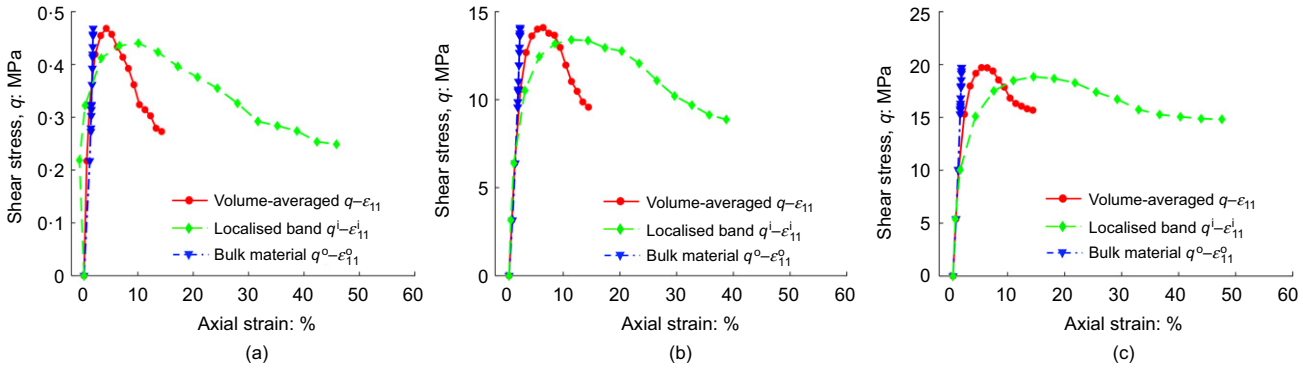

Fig. 8. Responses inside and outside the localisation band: (a) σ_{33}= 0·1 MPa; (b) σ_{33}= 4 MPa; (c) σ_{33}= 7 MPa

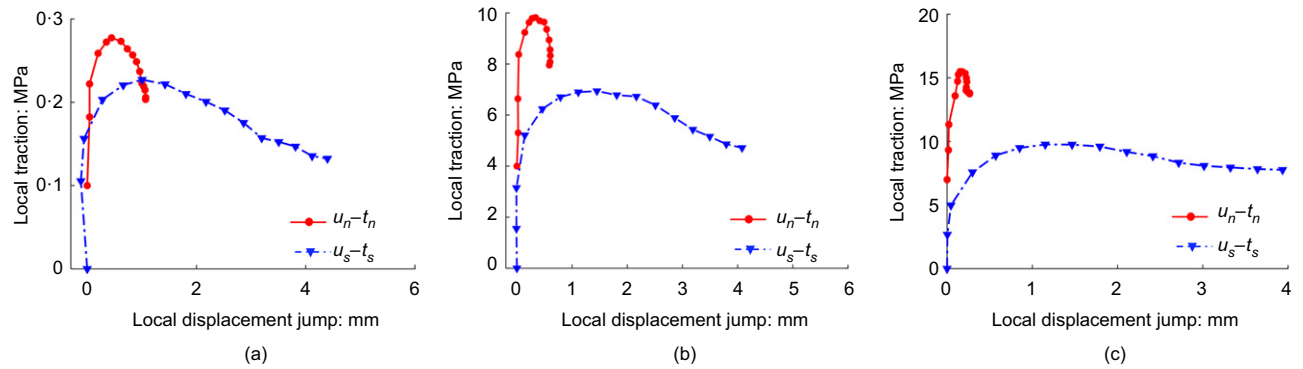

Fig. 9. Displacement jump–traction behaviour in the local coordinate system of the localisation band: (a) σ_{33}= 0·1 MPa; (b) σ_{33}= 4 MPa; (c) σ_{33}= 7 MPa

height of 100 mm, under two confining stresses, $\sigma_{33} =$ 50 and 150 kPa. Given void ratio $e = 0{\cdot}66$ and Poisson's ratio = 0·2, the parameter κ in each case is calculated as $\kappa =$ 0·017 and 0·011, respectively. Based on the volumetric strain contour in Takano *et al.* (2015), the thicknesses of the localisation bands are taken as $h = 20$ and 21 mm, while their orientations are $\theta = 55°$ and 50°, respectively.

The obtained shear stress plotted against shear strain ($\varepsilon_s = \sqrt{4J_2'/3}$ with J_2' being the second deviatoric strain invariant) in Fig. 11 indicates a clear difference between the volume-averaged responses and that of the localisation band. Three sets of volumetric strains, obtained from analysing the experimental data and plotted in Fig. 12, also reveal the dilatant trend inside the localisation band. This is consistent with the incremental volume strain fields measured by DIC (insets between dashed lines in Fig. 12). The obtained shear strains plotted in Figs 13(a) and 14(a) show that the shear deformation of the localisation band increases quickly, while the shear strain of the bulk material decreases due to relaxation. Since the thickness of the localisation band is assumed to be constant throughout the analysis and the deformation inside the band is

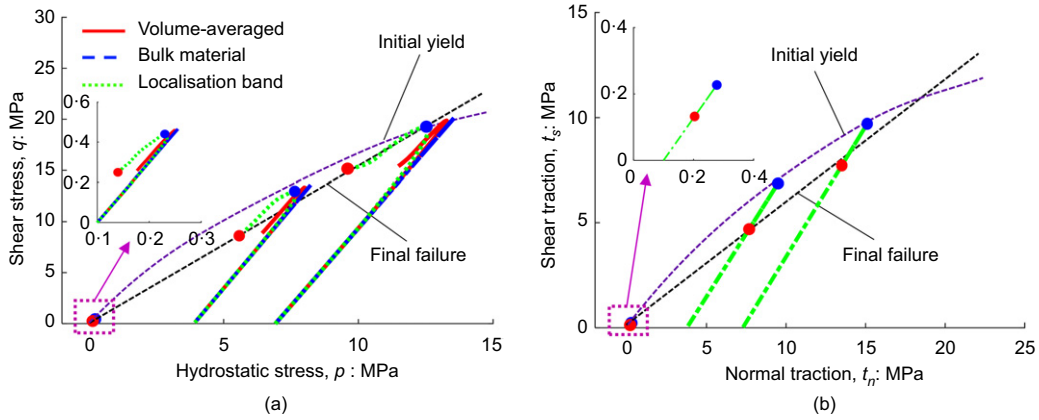

Fig. 10. Stress paths: (a) p–q stress paths; (b) t_n–t_s paths

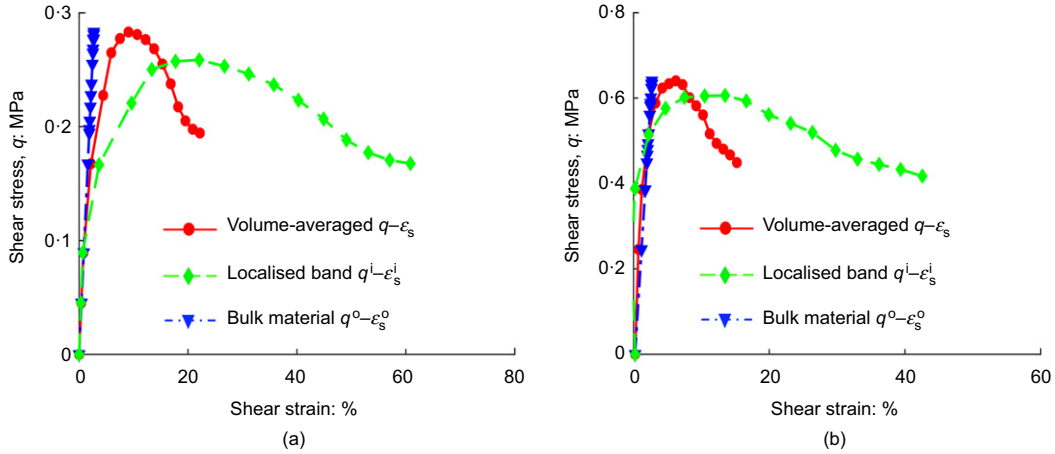

Fig. 11. Responses inside and outside the localisation band: (a) σ_{33}= 50 kPa; (b) σ_{33}= 150 kPa

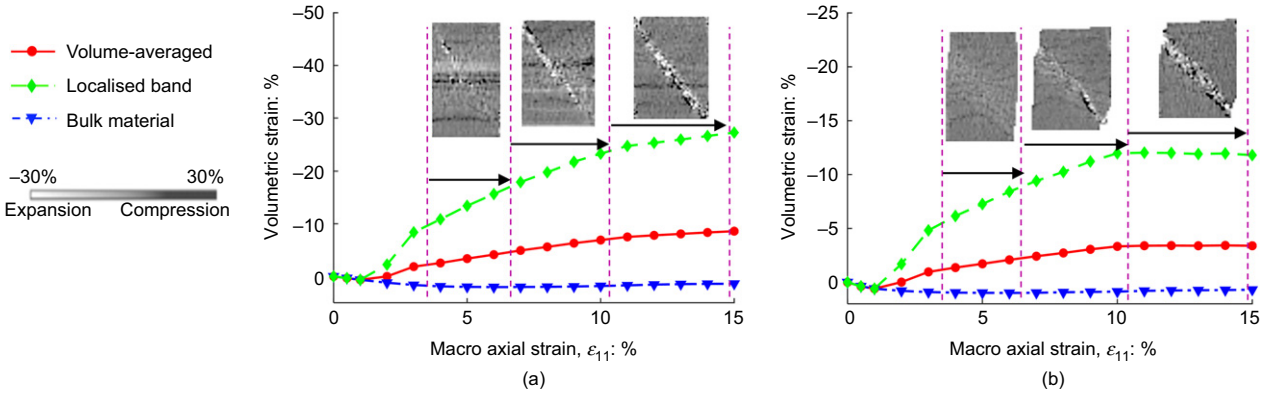

Fig. 12. Volumetric strains inside and outside the localisation band: (a) σ_{33}= 50 kPa; (b) σ_{33}= 150 kPa, alongside incremental volumetric strain fields measured by DIC (Takano *et al.*, 2015)

assumed to be uniform, there are discrepancies between the experimentally measured strain and that obtained using the proposed framework (see Figs 13(b) and 14(b)). Nonetheless, the deformation profiles obtained and those from experiments are comparable, especially when the localisation band becomes clear in later stages of the experiment (i.e. increments B–C and C–D).

The traction–displacement jump responses obtained, which are plotted in Figs 15(a) and 15(b), show that both normal and shear tractions exhibit non-linear behaviour before the softening phase. The normal–shear displacement jump relationship, plotted in Fig. 15(c), confirms the dilation of the localisation band presented earlier in Fig. 12. The figure also shows a decrease of dilation when confinement increases, as expected. Fig. 16(a) shows the deviation of stress paths in triaxial stress space, together with the paths of traction inside the localisation band (Fig. 16(b)), which can all be used to formulate a loading function of a continuum model to capture intrinsic material behaviour.

Analysing data from tests by Wong et al. (1997)

The data analysed in this section were acquired from experiments on Adamswiller sandstone samples having a diameter of 18·4 mm and a length of 38·1 mm, under three confining pressure levels, $\sigma_{33} = 5$, 20 and 40 MPa. The band orientations in three cases are recorded to be $\theta =$ 57°, 40° and 30°. The thickness of the localisation band is taken as $h = 2$ mm. The material elastic modulus under each confinement is calculated as $K = 35$, 39 and 39 GPa. As explained in the derivation of equations (12) and (13), since the thickness of the localisation band in this case is very small, the local axial stress in the band direction, σ_s^i, is assumed to be unchanged beyond the elastic range.

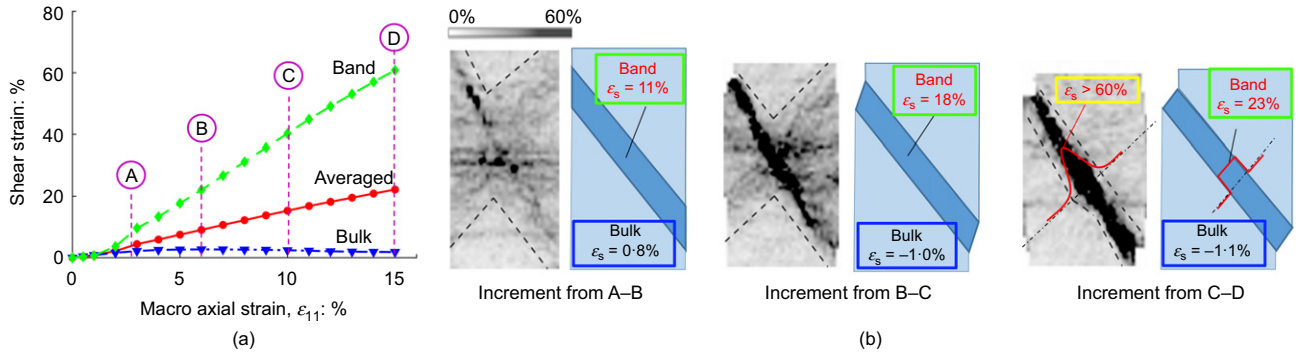

Fig. 13. Shear strain with respect to macro axial strain for σ_{33}= 50 kPa: (a) strain inside and outside the localisation band; (b) shear strain distribution, together with results from DIC (Takano *et al.*, 2015)

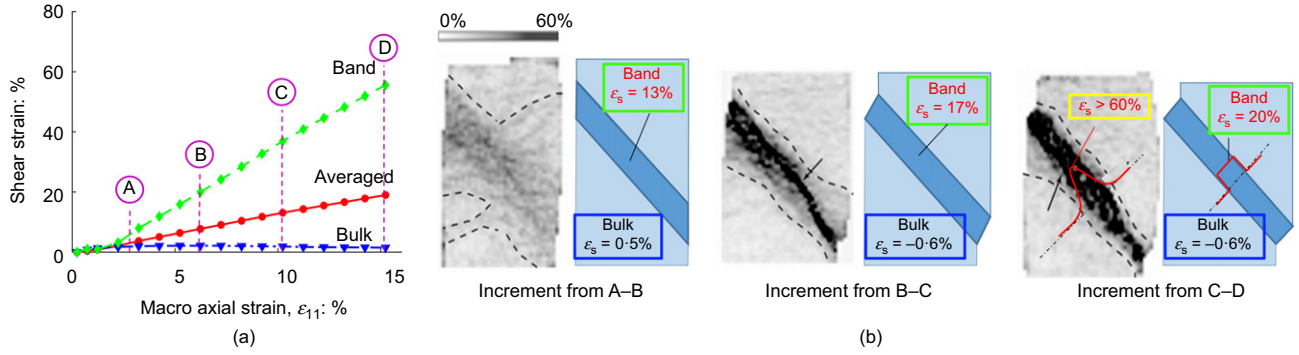

Fig. 14. Shear strain with respect to macro axial strain for σ_{33}= 150 kPa: (a) strain inside and outside the localisation band; (b) shear strain distribution, together with results from DIC (Takano *et al.*, 2015)

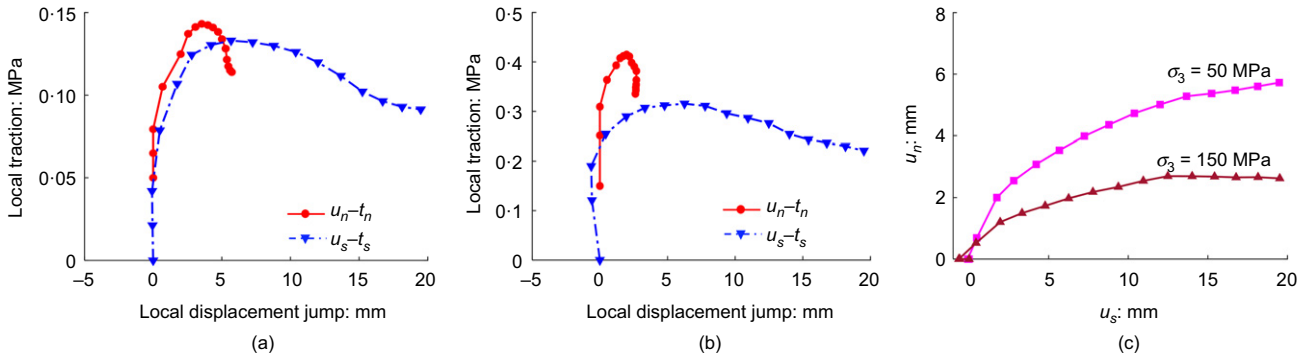

Fig. 15. Behaviour inside the localisation band: (a), (b) traction–displacement jump in the local coordinate system for σ_{33}= 50 and 150 kPa, respectively, and (c) local shear–normal displacement jumps

The volumetric strain obtained, plotted in Fig. 17, shows that after the homogeneous deformation stage, the volumetric strain inside the localisation band varies significantly. This is because the thickness of the localisation band is very small and thus its strain becomes sensitive to the displacement. The figure shows a dilation trend inside the localisation band under low confinement and a compaction trend under higher confining pressures, as expected. The large deformation of the localisation band can also be seen in the shear stress–axial strain curves in Fig. 18. The traction–displacement jump behaviour of the localisation band, presented in Fig. 19, further confirms the expansion/compaction behaviour in the post-peak stage.

Verification against synthetic data from numerical simulation

Since current experimental techniques are unable to obtain stress fields in the localisation band, verification of the proposed approach is performed against results from numerical experiments. To this end, the results from a numerical experiment using the authors' earlier model (Le *et al*, 2018), with an embedded localisation zone idealised as a cohesive-frictional surface, are used as synthetic experimental data to be analysed using the proposed approach. These synthetic results were validated against experimental data of triaxial compression testing on Bentheim sandstone under a confining pressure $\sigma_{33} = 10$ MPa, details of which can be found in Le *et al.* (2018).

For verification, the proposed approach requires macro strain increments ($\delta\varepsilon_{11}$, $\delta\varepsilon_{v}$) and the stress increment of the bulk material ($\delta\boldsymbol{\sigma}_{o}$) from the numerical experiment above to obtain the behaviour inside the localisation band. Fig. 20(a) shows good agreement between the behaviour obtained using the proposed approach and that by the numerical experiment. This verifies the accuracy of the proposed approach in analysing localised failure and experimental data for

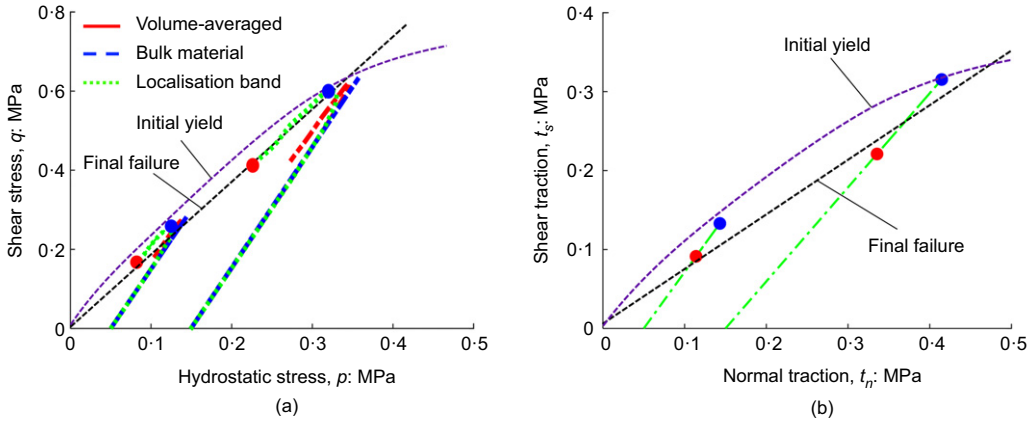

Fig. 16. Stress paths: (a) p–q stress paths and (b) t_n–t_s paths

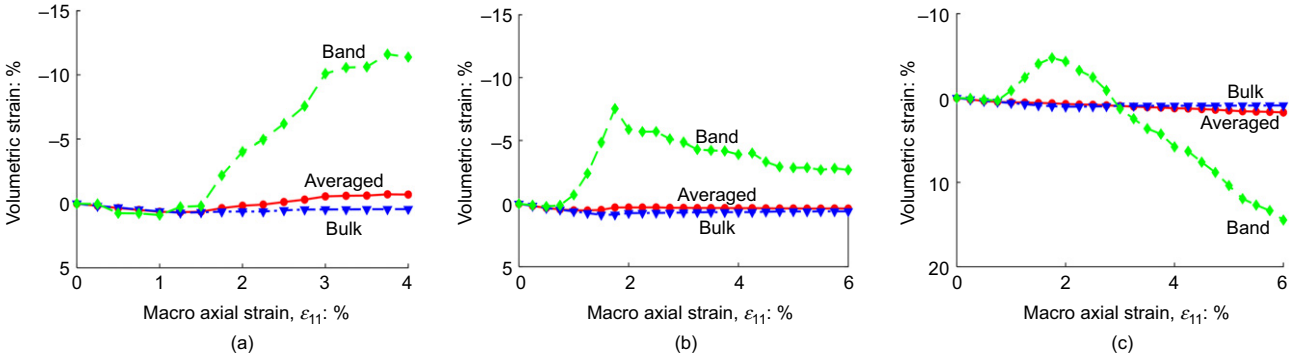

Fig. 17. Volumetric strain obtained from the analyses: (a) σ_{33}= 5 MPa; (b) σ_{33}= 20 MPa; (c) σ_{33}= 40 MPa

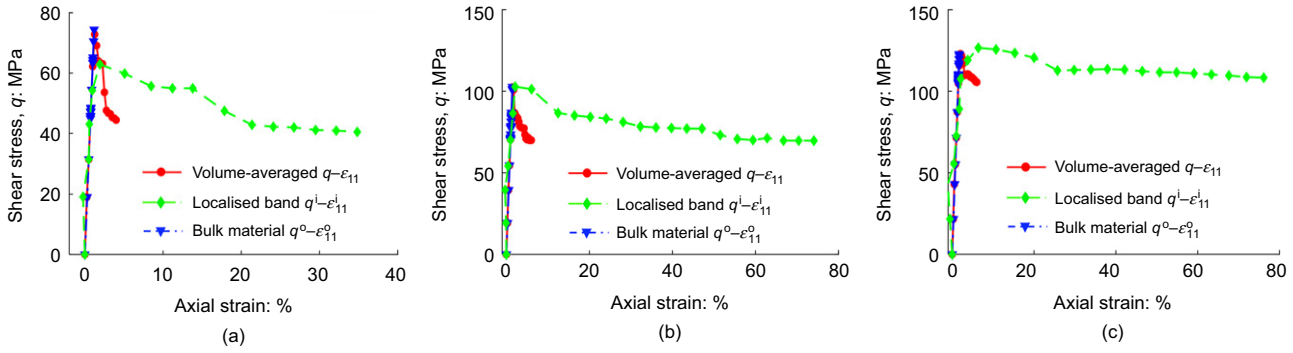

Fig. 18. Shear stress with respect to axial strain inside and outside the localisation band: (a) σ_{33}= 5 MPa; (b) σ_{33}= 20 MPa; (c) σ_{33}= 40 MPa

behaviour inside the localisation band. Employing the assumption on local stress increment of a band of finite thickness (see Fig. 4 with $h = 4$ mm), the proposed approach can result in the triaxiality condition inside the localisation band. Fig. 20(b) shows a clear distinction between the behaviour inside the localisation band, which can be considered as intrinsic material responses, and the volume-averaged behaviour of the whole specimen, which is usually considered in existing experiments as macro stress in triaxial tests.

The above results are based on the assumption that the thickness of the localisation band is not evolving during deformation. However, both experiments and discrete-element method (DEM) simulations (e.g. Alikarami *et al.*, 2015; Kawamoto *et al*, 2018; Verma *et al*, 2019) show that the localisation band thickness does not remain constant, but evolves under loading. In addition, the stress and deformation are not uniform, but vary inside the localisation band, which adds more difficulties in determining the thickness of the band. This makes it hard (or even impossible) at present to have a good correlation between the stresses inside the localisation band obtained using the proposed approach and those from numerical simulation using DEM. Although a theoretical approach taking into account the evolving thickness of the localisation band has been proposed in the authors' recent work (Nguyen & Bui, 2020), these issues still require further theoretical development and investigation.

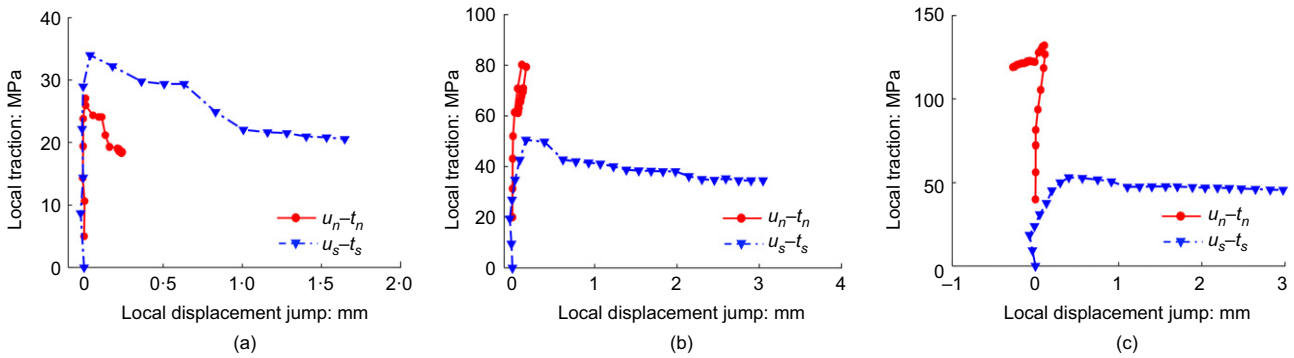

Fig. 19. Displacement jump – traction behaviour in the local coordinate system of the localisation band: (a) σ_{33}= 5 MPa; (b) σ_{33}= 20 MPa; (c) σ_{33}= 40 MPa

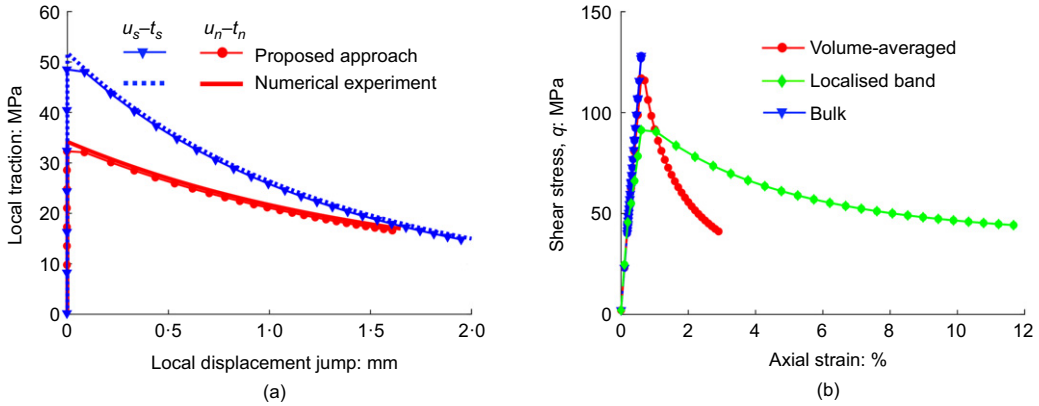

Fig. 20. Verification of the proposed approach against numerical experiment: (a) traction–displacement jump behaviour and (b) stress–axial strain for finite thickness band, h= 4 mm

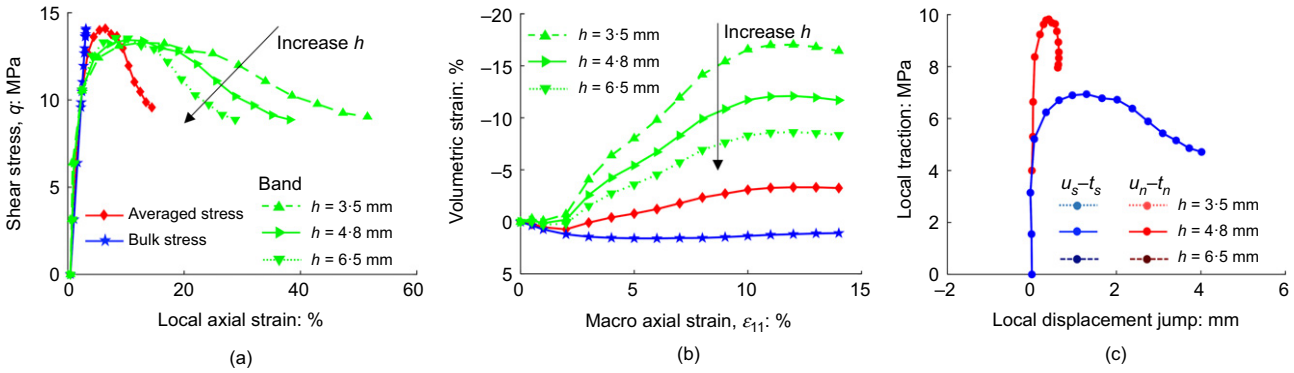

Fig. 21. Effect of shear band thickness on the obtained behaviour: (a) shear stress–axial strain; (b) volumetric strain–axial strain; (c) traction–displacement jump behaviour

PARAMETRIC STUDY AND IMPLICATION ON CONSTITUTIVE MODELLING

A parametric study is performed on the experimental data of Ottawa sand under confining stress $\sigma_{33} = 4$ MPa (previous section entitled 'Analysing data from tests by Alikarami *et al.* (2015)') with different values of thickness, $h =$ 3·5, 4·8 and 6·5 mm, to investigate its influence on the results obtained. The results plotted in Figs 21(a) and 21(b) show that an increase of the band thickness leads to a decrease in the magnitudes of strain inside the localisation band (i.e. both axial and volumetric strain), while the behaviour of the bulk material and the traction–displacement jump responses of the localisation band are unchanged. Given the same displacement jump, it is understandable that the strains inside the localisation band increase with the decrease in the band thickness. Since the size of the band is taken into account when calculating volume-averaged strain, as seen in equation (2), the volume-averaged strain obtained is unchanged. This parametric study indicates the interdependence of mechanical behaviour and thickness of the localisation band, as also explained in Nguyen & Houlsby (2007), Nguyen & Korsunsky (2008) and Nguyen *et al.* (2014).

A parametric study on the effect of localisation band orientation on the results obtained is then performed on the same set of data. The results, plotted in Fig. 22, show that an increase in the orientation of the band leads to a decrease in strain (Figs 22(a) and 22(b)) and displacement jumps inside the localisation band (Fig. 22(c)). This is reasonable because, given the same axial displacement, an increase in the orientation of the band leads to larger volume fractions and consequently a decrease of displacement jumps, calculated by equations (8) and (9). As a result, both stress–strain and traction–displacement jump responses significantly change with the change of the orientation. These results of parametric studies on the thickness and orientation of the localisation band emphasise the importance of these inputs to obtain reliable results.

To further illustrate the difference of the proposed approach and conventional ones in data analysis, the obtained shear and hydrostatic responses of the localisation band for the case of Ottawa sand under confinement of 4 MPa (see earlier section entitled 'Analysing data from tests by Alikarami *et al.* (2015)') are now plotted in Fig. 23, alongside those by conventional interpretation. As shown in the figure, both shear strain, $\varepsilon_s = \sqrt{4J_2'/3}$ and volumetric strain inside the localisation band are much larger than the averaged behaviour, which is usually interpreted as intrinsic material behaviour and used for the development of constitutive models.

A better modelling approach, to the best of the current authors' knowledge, should accommodate the difference in behaviour of the localisation band and its outer bulk material (see Figs 23(c) and 23(d)). Specifically, for failures involving thin localisation bands (e.g. sandstone), the triaxiality condition might not be well reflected inside the band (see discussions below equations (12) and (13)). Therefore, constitutive modelling frameworks, in this case, should be based on a cohesive-frictional model embedded in a volume element, since they require only normal and shear tractions on the boundary of the localisation band (e.g. Nguyen *et al.*, 2014; Mir *et al.*, 2015; Le *et al.*, 2017, 2018, 2019; Mir, 2017;

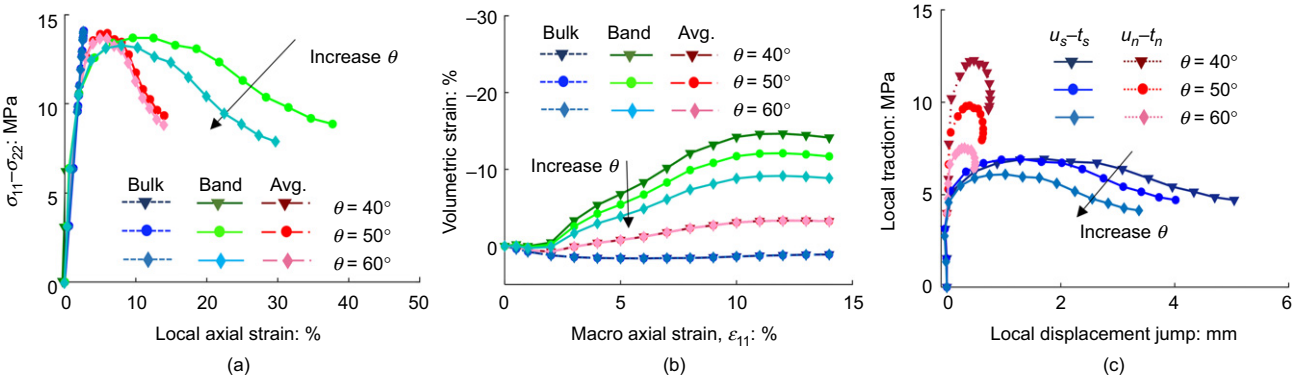

Fig. 22. Effect of shear band orientation on the obtained behaviour: (a) differential stress–axial strain; (b) volumetric strain–axial strain; (c) traction–displacement jump behaviour

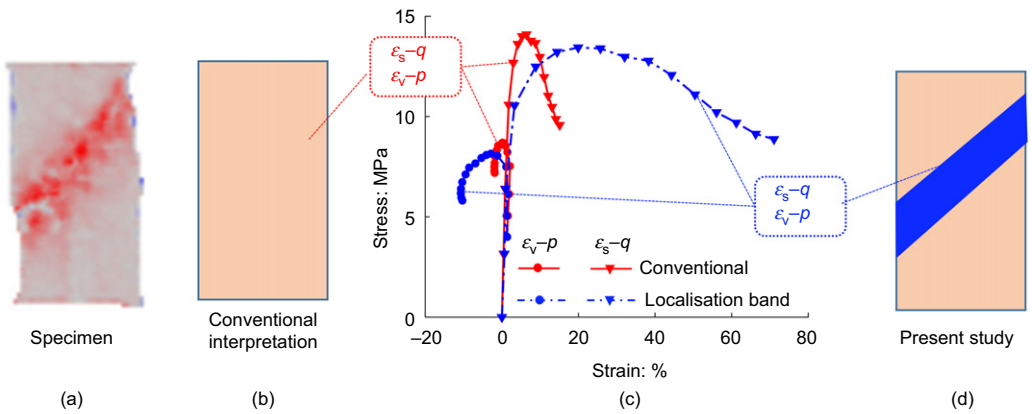

Fig. 23. Illustration of different schemes for data analysing and modelling: (a) specimen failure in experiments; (b) conventional interpretation; (c) shear and volumetric responses by the conventional approach and by the proposed scheme; (d) proposed schematic model

Tran *et al*., 2019; Wang *et al*., 2019). In contrast, for soils with no cohesion, the thickness of the localisation band, although small, is still significant and hence can result in a stress state inside the band closer to triaxial conditions (see examples in the earlier sections entitled 'Analysing data from tests by Alikarami *et al*. (2015)' and 'Analysing data from tests by Takano *et al*. (2015)'). As a result, a framework with a continuum constitutive model for the behaviour inside the band is a more reasonable choice to capture the material behaviour in this case (e.g. Nguyen *et al*., 2016a, 2016b; Nguyen & Bui, 2020). In both cases, the detailed evolution of stress and deformation inside the localisation band, obtained by the proposed framework, are crucial for calibration of such types of constitutive models.

CONCLUSIONS

This study proposes a new approach to the interpretation and analysis of experimental data that involves localised failure of geomaterials. The connection between meso behaviour of the localisation band and averaged responses of the whole specimen is employed for the analysis of experimental data involving localised failure. This provides a simple yet effective means to correctly obtain the evolution of both stress and deformation inside the localisation band, which are not measurable in standard experiments. The results obtained from the analysis of triaxial test data show that the true material behaviour, mostly taking place inside the localisation band, is far different from the macro volume-averaged responses that are usually and incorrectly considered as material behaviour.

The relationship between stress acting on the boundary of the localisation band and the relative displacements between its two sides is shown to be unique regardless of the localisation thickness and hence is free from the assumption of non-evolving band thickness. This constitutive relationship can well describe the behaviour of the localisation band in appropriate cases (i.e. a thin shear band). Also, while specimen specification in existing testing standards is suitable to yield simple failure modes for understanding material behaviour, the distinction between behaviour inside and outside the localisation band suggests more loading paths should be investigated to explore the material responses fully. This will be a necessity for both understanding and development of constitutive models.

ACKNOWLEDGEMENTS

The authors gratefully acknowledge support from the Australian Research Council by way of Discovery Projects FT140100408 (Nguyen), DP170103793 (Nguyen, Bui and Andrade) and DP190102779 (Bui and Nguyen).

APPENDIX. MESO–MACRO CONNECTIONS

Based on the fundamental relationships in the section entitled 'Fundamental relationships', this Appendix presents the calculation of quantities at macro-scale (volume-averaged) from those at meso-scale and vice versa. To this end, the behaviour inside and outside the localisation band is considered as homogeneous, with the constitutive stress–strain relationships written as

$$\delta\boldsymbol{\sigma}^{\mathrm{o}} = \boldsymbol{D}^{\mathrm{o}} : \delta\boldsymbol{\varepsilon}^{\mathrm{o}} \tag{14}$$

$$\delta\boldsymbol{\sigma}^{\mathrm{i}} = \boldsymbol{D}^{\mathrm{i}} : \delta\boldsymbol{\varepsilon}^{\mathrm{i}} \tag{15}$$

in which $\boldsymbol{D}^{\mathrm{o}}$ and $\boldsymbol{D}^{\mathrm{i}}$ are the tangent stiffness of the materials outside and inside the localisation band, respectively.

CALCULATING MACRO BEHAVIOUR FROM MESO RESPONSES

Given the stress and strain increments of the localisation band (i.e. $\delta\boldsymbol{\varepsilon}^{\mathrm{i}}$ and $\delta\boldsymbol{\sigma}^{\mathrm{i}}$), alongside its thickness and orientation, the macro responses and other quantities of the specimen can be calculated. Substituting equations (1) and (14) into the incremental form traction continuity $\delta\boldsymbol{t}^{\mathrm{i}} = \delta\boldsymbol{t}^{\mathrm{o}}$ and solving for $\delta\boldsymbol{u}$, one obtains

$$\delta\boldsymbol{u} = h(\boldsymbol{n}\cdot\boldsymbol{D}^{\mathrm{o}}\cdot\boldsymbol{n})^{-1}\left(\boldsymbol{D}^{\mathrm{o}} : \delta\boldsymbol{\varepsilon}^{\mathrm{i}}\cdot\boldsymbol{n} - \delta\boldsymbol{\sigma}^{\mathrm{i}}\cdot\boldsymbol{n}\right) \tag{16}$$

This equation is then substituted into equations (1) and (14) to obtain the strain and stress of the surrounding bulk material

$$\delta\boldsymbol{\varepsilon}^{\mathrm{o}} = \delta\boldsymbol{\varepsilon}^{\mathrm{i}} - \left[\boldsymbol{n}\otimes(\boldsymbol{n}\cdot\boldsymbol{D}^{\mathrm{o}}\cdot\boldsymbol{n})^{-1}\left(\boldsymbol{D}^{\mathrm{o}} : \delta\boldsymbol{\varepsilon}^{\mathrm{i}}\cdot\boldsymbol{n} - \delta\boldsymbol{\sigma}^{\mathrm{i}}\cdot\boldsymbol{n}\right)\right]^{s} \tag{17}$$

$$\begin{aligned}\delta\boldsymbol{\sigma}^{\mathrm{o}} =& \boldsymbol{D}^{\mathrm{o}} : \delta\boldsymbol{\varepsilon}^{\mathrm{o}} = \boldsymbol{D}^{\mathrm{o}} : \\ & \left\{\delta\boldsymbol{\varepsilon}^{\mathrm{i}} - \left[\boldsymbol{n}\otimes(\boldsymbol{n}\cdot\boldsymbol{D}^{\mathrm{o}}\cdot\boldsymbol{n})^{-1}\left(\boldsymbol{D}^{\mathrm{o}} : \delta\boldsymbol{\varepsilon}^{\mathrm{i}}\cdot\boldsymbol{n} - \delta\boldsymbol{\sigma}^{\mathrm{i}}\cdot\boldsymbol{n}\right)\right]^{s}\right\}\end{aligned} \tag{18}$$

Finally, the macro stress and strain can be calculated from equations (4) and (2) as

$$\begin{aligned}\delta\boldsymbol{\sigma} =& f\,\delta\boldsymbol{\sigma}^{\mathrm{i}} + (1-f)\boldsymbol{D}^{\mathrm{o}} : \\ & \left\{\delta\boldsymbol{\varepsilon}^{\mathrm{i}} - \left[\boldsymbol{n}\otimes(\boldsymbol{n}\cdot\boldsymbol{D}^{\mathrm{o}}\cdot\boldsymbol{n})^{-1}\left(\boldsymbol{D}^{\mathrm{o}} : \delta\boldsymbol{\varepsilon}^{\mathrm{i}}\cdot\boldsymbol{n} - \delta\boldsymbol{\sigma}^{\mathrm{i}}\cdot\boldsymbol{n}\right)\right]^{s}\right\}\end{aligned} \tag{19}$$

$$\delta\boldsymbol{\varepsilon} = \delta\boldsymbol{\varepsilon}^{\mathrm{i}} - (1-f)\left[\boldsymbol{n}\otimes(\boldsymbol{n}\cdot\boldsymbol{D}^{\mathrm{o}}\cdot\boldsymbol{n})^{-1}\left(\boldsymbol{D}^{\mathrm{o}} : \delta\boldsymbol{\varepsilon}^{\mathrm{i}}\cdot\boldsymbol{n} - \delta\boldsymbol{\sigma}^{\mathrm{i}}\cdot\boldsymbol{n}\right)\right]^{s} \tag{20}$$

OBTAINING MESO RESPONSES FROM MACRO BEHAVIOUR

Given the macro stress and strain increments (i.e. $\delta\boldsymbol{\varepsilon}$ and $\delta\boldsymbol{\sigma}$), the quantities inside and outside the localisation band can also be calculated. Substituting equation (1) into equation (2), one obtains

$$\delta\boldsymbol{\varepsilon}^{\mathrm{o}} = \delta\boldsymbol{\varepsilon} - \frac{f}{h}(\boldsymbol{n}\otimes\delta\boldsymbol{u})^{s} \tag{21}$$

Substituting equations (14) and (21) into equation (4), one obtains

$$\delta\boldsymbol{\sigma}^{\mathrm{i}} = \frac{1}{f}\left\{\delta\boldsymbol{\sigma} - (1-f)\boldsymbol{D}^{\mathrm{o}} : \left[\delta\boldsymbol{\varepsilon} - \frac{f}{h}(\boldsymbol{n}\otimes\delta\boldsymbol{u})^{s}\right]\right\} \tag{22}$$

Substituting this into the incremental form of traction continuity in equation (3), $\delta\boldsymbol{t} = \delta\boldsymbol{t}^{\mathrm{i}}$, $\delta\boldsymbol{u}$ can be calculated as

$$\delta\boldsymbol{u} = \frac{h}{f}(\boldsymbol{n}\cdot\boldsymbol{D}^{\mathrm{o}}\cdot\boldsymbol{n})^{-1}(\boldsymbol{D}^{\mathrm{o}} : \delta\boldsymbol{\varepsilon} - \delta\boldsymbol{\sigma})\cdot\boldsymbol{n} \tag{23}$$

From equations (21) and (23), the strain and stress increments of the surrounding bulk material are calculated as

$$\delta\boldsymbol{\varepsilon}^{\mathrm{o}} = \delta\boldsymbol{\varepsilon} - \left[\boldsymbol{n}\otimes(\boldsymbol{n}\cdot\boldsymbol{D}^{\mathrm{o}}\cdot\boldsymbol{n})^{-1}(\boldsymbol{D}^{\mathrm{o}} : \delta\boldsymbol{\varepsilon} - \delta\boldsymbol{\sigma})\cdot\boldsymbol{n}\right]^{s} \tag{24}$$

$$\begin{aligned}\delta\boldsymbol{\sigma}^{\mathrm{o}} =& \boldsymbol{D}^{\mathrm{o}} : \delta\boldsymbol{\varepsilon}^{\mathrm{o}} = \boldsymbol{D}^{\mathrm{o}} : \\ & \left\{\delta\boldsymbol{\varepsilon} - \left[\boldsymbol{n}\otimes(\boldsymbol{n}\cdot\boldsymbol{D}^{\mathrm{o}}\cdot\boldsymbol{n})^{-1}(\boldsymbol{D}^{\mathrm{o}} : \delta\boldsymbol{\varepsilon} - \delta\boldsymbol{\sigma})\cdot\boldsymbol{n}\right]^{s}\right\}\end{aligned} \tag{25}$$

The stress and strain increments of the localisation band can then be calculated from the bulk and the overall quantities as

$$\delta\boldsymbol{\sigma}^{\mathrm{i}} = \frac{\delta\boldsymbol{\sigma} - (1-f)\delta\boldsymbol{\sigma}^{\mathrm{o}}}{f} \tag{26}$$

$$\delta\boldsymbol{\varepsilon}^{\mathrm{i}} = \frac{\delta\boldsymbol{\varepsilon} - (1-f)\delta\boldsymbol{\varepsilon}^{\mathrm{o}}}{f} \tag{27}$$

NOTATION

A, f	surface area and volume fraction of localisation band
$\boldsymbol{D}^{\mathrm{o}}$	elastic tangent stiffness
h, θ	thickness and orientation of localisation band
I_1	first invariant of stress tensor
J_2	second invariant of deviatoric stress tensor
K, G	bulk and shear elastic modulus
$\boldsymbol{n}$	normal vector of localisation band
p, q	hydrostatic and deviatoric pressure
$\mathbf{R}$	transformation matrix from global to local coordinate system
$\boldsymbol{t}$	overall traction of specimen in global coordinate system
$\boldsymbol{t}^{\mathrm{i}}$	traction of localisation band in global coordinate system
$\boldsymbol{t}^{\mathrm{i}}_{\mathrm{local}} = [\, t_n \quad t_s \quad t_t \,]^{\mathrm{T}}$	traction of localisation band in local coordinate system
$\boldsymbol{t}^{\mathrm{o}}$	traction of bulk material in global coordinate system
$\boldsymbol{u}$	displacement jump of localisation band in global coordinate system
$\boldsymbol{u}_{\mathrm{local}} = [\, u_n \quad u_s \quad u_t \,]^{\mathrm{T}}$	displacement jump of localisation band in local coordinate system
$\boldsymbol{\varepsilon} = [\varepsilon_{11}\ \varepsilon_{22}\ \varepsilon_{33}\ \gamma_{12}\ \gamma_{23}\ \gamma_{31}]^{\mathrm{T}}$	volume-averaged strain of specimen
$\boldsymbol{\varepsilon}^{\mathrm{i}} = [\varepsilon^{\mathrm{i}}_{11}\ \varepsilon^{\mathrm{i}}_{22}\ \varepsilon^{\mathrm{i}}_{33}\ \varepsilon^{\mathrm{i}}_{12}\ \varepsilon^{\mathrm{i}}_{23}\ \varepsilon^{\mathrm{i}}_{31}]^{\mathrm{T}}$	strain inside the localisation band
$\boldsymbol{\varepsilon}^{\mathrm{o}} = [\varepsilon^{\mathrm{o}}_{11}\ \varepsilon^{\mathrm{o}}_{22}\ \varepsilon^{\mathrm{o}}_{33}\ \varepsilon^{\mathrm{o}}_{12}\ \varepsilon^{\mathrm{o}}_{23}\ \varepsilon^{\mathrm{o}}_{31}]^{\mathrm{T}}$	strain of outer bulk material
$\varepsilon_{\mathrm{s}}, \varepsilon_{\mathrm{v}}$	shear and volumetric strain
v	specific volume change
$\boldsymbol{\sigma} = [\sigma_{11}\ \sigma_{22}\ \sigma_{33}\ \sigma_{12}\ \sigma_{23}\ \sigma_{31}]^{\mathrm{T}}$	volume-averaged stress in global coordinate system
$\boldsymbol{\sigma}^{\mathrm{i}} = [\sigma^{\mathrm{i}}_{11}\ \sigma^{\mathrm{i}}_{22}\ \sigma^{\mathrm{i}}_{33}\ \sigma^{\mathrm{i}}_{12}\ \sigma^{\mathrm{i}}_{23}\ \sigma^{\mathrm{i}}_{31}]^{\mathrm{T}}$	stress inside localisation band
$\boldsymbol{\sigma}_{\mathrm{local}} = [\sigma_n\ \sigma_s\ \sigma_t\ \sigma_{ns}\ \sigma_{st}\ \sigma_{nt}]^{\mathrm{T}}$	volume-averaged stress in local coordinate system
$\boldsymbol{\sigma}^{\mathrm{o}} = [\sigma^{\mathrm{o}}_{11}\ \sigma^{\mathrm{o}}_{22}\ \sigma^{\mathrm{o}}_{33}\ \sigma^{\mathrm{o}}_{12}\ \sigma^{\mathrm{o}}_{23}\ \sigma^{\mathrm{o}}_{31}]^{\mathrm{T}}$	stress of bulk material
v, n	Poisson's ratio and material porosity

REFERENCES

Alikarami, R., Andò, E., Gkiousas-Kapnisis, M., Torabi, A. & Viggiani, G. (2015). Strain localisation and grain breakage in sand under shearing at high mean stress: insights from in situ X-ray tomography. *Acta Geotech.* **10**, No. 1, 15–30, https://doi.org/10.1007/s11440-014-0364-6.

Alshibli, K. A., Jarrar, M. F., Druckrey, A. M. & Al-Raoush, R. I. (2017). Influence of particle morphology on 3D kinematic behavior and strain localization of sheared sand. *J. Geotech. Geoenviron. Engng* **143**, No. 2, 04016097, https://doi.org/10.1061/(ASCE)GT.1943-5606.0001601.

Amirrahmat, S., Alshibli, K. A., Jarrar, M. F., Zhang, B. & Regueiro, R. A. (2018). Equivalent continuum strain calculations based on 3D particle kinematic measurements of sand. *Int. J. Numer. Analyt. Methods Geomech.* **42**, No. 8, 999–1015, https://doi.org/10.1002/nag.2779.

Amirrahmat, S., Druckrey, A. M., Alshibli, K. A. & Al-Raoush, R. I. (2019). Micro shear bands: precursor for strain localization in sheared granular materials. *J. Geotech. Geoenviron. Engng* **145**, No. 2, 04018104, https://doi.org/10.1061/(ASCE)GT.1943-5606.0001989.

Dawidowski, P., Dullona, C., Naimi, Z. & Zamparelli, M. (2015). *Analysis of strain localisation in Hawkesbury sandstone under uniaxial compression using digital image correlation techniques.* Adelaide, Australia: University of Adelaide.

Desrues, J., Chambon, R., Mokni, M. & Mazerolle, F. (1996). Void ratio evolution inside shear bands in triaxial sand specimens studied by computed tomography. *Géotechnique* **46**, No. 3, 529–546, https://doi.org/10.1680/geot.1996.46.3.529.

Desrues, J., Andò, E., Mevoli Ando, F. A., Debove, L. & Viggiani, G. (2018). How does strain localise in standard triaxial tests on sand: revisiting the mechanism 20 years on. *Mech. Res. Communs* **92**, 142–146, https://doi.org/10.1016/j.mechrescom.2018.08.007.

Druckrey, A. M., Alshibli, K. A. & Al-Raoush, R. I. (2018). Discrete particle translation gradient concept to expose strain localisation in sheared granular materials using 3D experimental kinematic measurements. *Géotechnique* **68**, No. 2, 162–170, https://doi.org/10.1680/jgeot.16.P.148.

Einav, I. (2007a). Breakage mechanics – part II: modelling granular materials. *J. Mech. Phys. Solids* **55**, No. 6, 1298–1320, https://doi.org/10.1016/j.jmps.2006.11.004.

Einav, I. (2007b). Breakage mechanics – part I: theory. *J. Mech. Phys. Solids* **55**, No. 6, 1274–1297, https://doi.org/10.1016/j.jmps.2006.11.003.

Haghighat, E. & Pietruszczak, S. (2015). On modeling of discrete propagation of localised damage in cohesive-frictional material. *Int. J. Numer. Analyt. Methods Geomech* **39**, No. 16, 1774–1790.

Haghighat, E. & Pietruszczak, S. (2016). On modeling of fractured media using an enhanced embedded discontinuity approach. *Extreme Mech. Lett.* **6**, 10–22, https://doi.org/10.1016/j.eml.2015.11.001.

Hill, R. (1963). Elastic properties of reinforced solids: some theoretical principles. *J. Mech. Phys. Solids* **11**, No. 5, 357–372, https://doi.org/10.1016/0022-5096(63)90036-X.

Kawamoto, R., Andò, E., Viggiani, G. & Andrade, J. E. (2018). All you need is shape: predicting shear banding in sand with LS-DEM. *J. Mech. Phys. Solids* **111**, 375–392, https://doi.org/10.1016/j.jmps.2017.10.003.

Le, L. A. (2019). *A mechanism-based approach to constitutive modelling of quasi-brittle geomaterials with and without fibre reinforcement*. PhD thesis, The University of Adelaide, Adelaide, Australia.

Le, L. A., Nguyen, G. D., Bui, H. H., Sheikh, A. H., Kotousov, A. & Khanna, A. (2017). Modelling jointed rock mass as a continuum with an embedded cohesive-frictional model. *Engng Geol.* **228**, 107–120, https://doi.org/10.1016/j.enggeo.2017.07.011.

Le, L. A., Nguyen, G. D., Bui, H. H., Sheikh, A. H. & Kotousove, A. (2018). Localised failure mechanism as the basis for constitutive modelling of geomaterials. *Int. J. Engng Sci.* **133**, 284–310.

Le, L. A., Nguyen, G. D., Bui, H. H., Sheikh, A. H. & Kotousov, A. (2019). Incorporation of micro-cracking and fibre bridging phenomena in constitutive modelling of fibre reinforced concrete. *J. Mech. Phys. Solids* **133**, 103732, https://doi.org/10.1016/j.jmps.2019.103732.

Lee, H. & Haimson, B. C. (2011). True triaxial strength, deformability, and brittle failure of granodiorite from the San Andreas fault observatory at depth. *Int. J. Rock Mech. Min. Sci.* **48**, No. 7, 1199–1207, https://doi.org/10.1016/j.ijrmms.2011.08.003.

Lommatzsch, M., Exner, U., Gier, S. & Grasemann, B. (2015). Dilatant shear band formation and diagenesis in calcareous, arkosic sandstones, Vienna Basin (Austria). *Mar. Pet. Geol.* **62**, 144–160, https://doi.org/10.1016/j.marpetgeo.2015.02.002.

Ma, X. & Haimson, B. C. (2016). Failure characteristics of two porous sandstones subjected to true triaxial stresses. *J. Geophys. Res. Solid Earth* **121**, No. 5, 6477–6498, https://doi.org/10.1002/2015JB012608.

Mir, A. (2017). *A thermodynamic approach to modelling brittle-ductile and localised failure of rocks using damage mechanics and plasticity theory.* PhD thesis, The University of Adelaide, Adelaide, Australia.

Mir, A., Nguyen, G. D. & Sheikh, A. H. (2015). A continuum model with an embedded fracture process zone modelled as a cohesive frictional interface. *Appl. Mech. Mater.* **846**, 360–365.

Moallemi, S. & Pietruszczak, S. (2017). Analysis of localized fracture in 3D reinforced concrete structures using volume averaging technique. *Finite Elem. Anal. Des.* **125**, 41–52, https://doi.org/10.1016/j.finel.2016.10.004.

Mohammadi, H. & Pietruszczak, S. (2019). Description of damage process in fractured rocks. *Int. J. Rock Mech. Min. Sci.* **113**, 295–302, https://doi.org/10.1016/j.ijrmms.2018.12.003.

Neilsen, M. K. & Schreyer, H. L. (1993). Bifurcations in elastic-plastic materials. *Int. J. Solids Structs* **30**, No. 4, 521–544, https://doi.org/10.1016/0020-7683(93)90185-A.

Nguyen, G. D. & Bui, H. H. (2020). A thermodynamics- and mechanism-based framework for constitutive models with

evolving thickness of localisation band. *Int. J. Solids Structs* **187**, 100–120.

Nguyen, G. D. & Houlsby, G. T. (2007). Non-local damage modelling of concrete: a procedure for the determination of parameters. *Int. J. Numer. Analyt. Methods Geomech.* **31**, No. 7, 867–891.

Nguyen, G. D. & Korsunsky, A. M. (2008). Development of an approach to constitutive modelling of concrete: isotropic damage coupled with plasticity. *Int. J. Solids Structs* **45**, No. 20, 5483–5501.

Nguyen, G. D., Einav, I. & Korsunsky, A. M. (2012). How to connect two scales of behaviour in constitutive modelling of geomaterials. *Géotechnique Lett.* **2**, No. 3, 129–134, https://doi.org/10.1680/geolett.12.00030.

Nguyen, G. D., Korsunsky, A. M. & Einav, I. (2014). A constitutive modelling framework featuring two scales of behaviour: fundamentals and applications to quasi-brittle failure. *Engng Fract. Mech.* **115**, 221–240, https://doi.org/10.1016/j.engfracmech.2013.11.006.

Nguyen, G. D., Nguyen, C., Nguyen, V. P., Bui, H. H. & Shen, L. (2016a). A size-dependent constitutive modelling framework for localised failure analysis. *Comput. Mech.* **58**, No. 2, 257–280, https://doi.org/10.1007/s00466-016-1293-z.

Nguyen, G. D., Nguyen, C. T., Bui, H. H. & Nguyen, V. P. (2016b). Constitutive modelling of compaction localisation in porous sandstones. *Int. J. Rock Mech. Min. Sci.* **83**, 57–72. https://doi.org/10.1016/j.ijrmms.2015.12.018.

Nguyen, C. T., Nguyen, G. D., Das, A. & Bui, H. H. (2017). Constitutive modelling of progressive localised failure in porous sandstones under shearing at high confining pressures. *Int. J. Rock Mech. Min. Sci* **93**, 179–195, https://doi.org/10.1016/j.ijrmms.2017.01.014.

Pietruszczak, S. & Haghighat, E. (2015). Modeling of deformation and localized failure in anisotropic rocks. *Int. J. Solids Structs* **67–68**, 93–101, https://doi.org/10.1016/j.ijsolstr.2015.04.004.

Pour, A. F., Nguyen, G. D., Vincent, T. & Ozbakkaloglu, T. (2020). Investigation of the compressive behavior and failure modes of unconfined and FRP-confined concrete using digital image correlation. *Comp. Structs* **252**, 112642.

Salvatore, E., Modoni, G., Andò, E., Albano, M. & Viggiani, G. (2017). Determination of the critical state of granular materials with triaxial tests. *Soils Found.* **57**, No. 5, 733–744, https://doi.org/10.1016/j.sandf.2017.08.005.

Takano, D., Lenoir, N., Otani, J. & Hall, S. A. (2015). Localised deformation in a wide-grained sand under triaxial compression revealed by X-ray tomography and digital image correlation. *Soils Found.* **55**, No. 4, 906–915, https://doi.org/10.1016/j.sandf.2015.06.020.

Tran, H. T., Wang, Y., Nguyen, G. D., Kodikara, J., Sanchez, M. & Bui, H. H. (2019). Modelling 3D desiccation cracking in clayey soils using a size-dependent SPH computational approach. *Comput. Geotech* **116**, 103209, https://doi.org/10.1016/j.compgeo.2019.103209.

Vachaparampil, A. & Ghassemi, A. (2017). Failure characteristics of three shales under true-triaxial compression. *Int. J. Rock Mech. Min. Sci* **100**, 151–159, https://doi.org/10.1016/j.ijrmms.2017.10.018.

Verma, R. K., Pour, A. F., Dawidowski, P., Nguyen, G. D., Bui, H. H., Karakus, M. & Taheri, A. (2019). Analysing localisation behaviour of rocks using digital image correlation technique. In *Proceedings of the 13th international conference on the mechanical behaviour of materials* (ed. R. Das), pp. 304–311. Red Hook, NY, USA: Curran Associates.

Wang, Y., Bui, H. H., Nguyen, G. D. & Ranjith, P. G. (2019). A new SPH-based continuum framework with an embedded fracture process zone for modelling rock fracture. *Int. J. Solids Structs* **159**, 40–57, https://doi.org/10.1016/j.ijsolstr.2018.09.019.

Wong, T.-F., David, C. & Zhu, W. (1997). The transition from brittle faulting to cataclastic flow in porous sandstones: mechanical deformation. *J. Geophys. Res. Solid Earth* **102**, No. B2, 3009–3025.

Wood, D. M. (1991). *Soil behaviour and critical state soil mechanics*. Cambridge, UK: Cambridge University Press.